Quantitative CEST imaging of amide proton transfer in acute ischaemic stroke

Y. Msayib[a], G.W.J. Harston[b], Y.K. Tee[c], F. Sheerin[b], N.P. Blockley[d], T.W. Okell[d], P. Jezzard[d], J. Kennedy[b], M.A. Chappell[a,d,*]

[a] Institute of Biomedical Engineering, Department of Engineering Science, University of Oxford, UK
[b] Acute Vascular Imaging Centre, Radcliffe Department of Medicine, University of Oxford, UK
[c] Department of Mechatronics and Biomedical Engineering, Lee Kong Chian Faculty of Engineering and Science, Universiti Tunku Abdul Rahman, Malaysia
[d] Wellcome Centre for Integrative Neuroimaging, FMRIB Division, Nuffield Department of Clinical Neurosciences, University of Oxford, UK

ARTICLE INFO

ABSTRACT

Background: Amide proton transfer (APT) imaging may help identify the ischaemic penumbra in stroke patients, the classical definition of which is a region of tissue around the ischaemic core that is hypoperfused and metabolically stressed. Given the potential of APT imaging to complement existing imaging techniques to provide clinically-relevant information, there is a need to develop analysis techniques that deliver a robust and repeatable APT metric. The challenge to accurate quantification of an APT metric has been the heterogeneous *in-vivo* environment of human tissue, which exhibits several confounding magnetisation transfer effects including spectrally-asymmetric nuclear Overhauser effects (NOEs). The recent literature has introduced various model-free and model-based approaches to analysis that seek to overcome these limitations.

Objectives: The objective of this work was to compare quantification techniques for CEST imaging that specifically separate APT and NOE effects for application in the clinical setting. Towards this end a methodological comparison of different CEST quantification techniques was undertaken in healthy subjects, and around clinical endpoints in a cohort of acute stroke patients.

Methods: MRI data from 12 patients presenting with ischaemic stroke were retrospectively analysed. Six APT quantification techniques, comprising model-based and model-free techniques, were compared for repeatability and ability for APT to distinguish pathological tissue in acute stroke.

Results: Robustness analysis of six quantification techniques indicated that the multi-pool model-based technique had the smallest contrast between grey and white matter (2%), whereas model-free techniques exhibited the highest contrast (> 30%). Model-based techniques also exhibited the lowest spatial variability, of which 4-pool APTR* was by far the most uniform (10% coefficient of variation, CoV), followed by 3-pool analysis (20%). Four-pool analysis yielded the highest ischaemic core contrast-to-noise ratio (0.74). Four-pool modelling of APT effects was more repeatable (3.2% CoV) than 3-pool modelling (4.6% CoV), but this appears to come at the cost of reduced contrast between infarct growth tissue and normal tissue.

Conclusion: The multi-pool measures performed best across the analyses of repeatability, spatial variability, contrast-to-noise ratio, and grey matter-white matter contrast, and might therefore be more suitable for use in clinical imaging of acute stroke. Addition of a fourth pool that separates NOEs and semisolid effects appeared to be more biophysically accurate and provided better separation of the APT signal compared to the 3-pool equivalent, but this improvement appeared be accompanied by reduced contrast between infarct growth tissue and normal tissue.

1. Introduction

AMIDE proton transfer (APT) imaging, where contrast originates from backbone amide protons of mobile proteins and peptides within cells resonating at 3.5 ppm downfield from water (Ward et al., 2000; Zhou et al., 2003), is the most developed of the endogenous CEST contrast modes (Li et al., 2015; Vinogradov et al., 2013). Quantification of APT exchange rate in brain tissue has been used to measure pH-related

---

changes associated with impaired metabolism and cell death, as intracellular pH is exchange rate-dependent (Tee et al., 2014). This is relevant to ischaemic stroke where a reduction in blood supply to brain tissue leads to impaired metabolism, where APT imaging may help identify the ischaemic penumbra in stroke patients (Harston et al., 2015), the classical definition of which is a region of tissue around the ischaemic core that is hypoperfused and metabolically stressed (Zhou et al., 2003; Sun et al., 2007; Astrup et al., 1981).

However, the challenge to accurate quantification of an APT metric has been the heterogeneous *in-vivo* environment of human tissue, which exhibits several confounding magnetisation transfer (MT) effects including spillover of direct water saturation, broadband magnetisation transfer from semisolid tissue, an overlapping of metabolite peaks due to their relatively broad spectra, as well as noise and artefact (Jin et al., 2013; Zhou et al., 2013).

Early APT studies tended to employ relatively simple measures of spectral asymmetry for quantification that assume a broad featureless spectrum upfield of water as a fixed reference. This assumption has been undermined by the realisation that the upfield spectrum is not a good reference for asymmetry techniques due to the relatively prominent asymmetric saturation effects in the aliphatic region of the spectrum from -2 to -5 ppm that are associated with intramolecular magnetisation transfer processes, referred to as nuclear Overhauser effects (NOEs).

The recent literature has introduced various approaches to CEST analysis that seek to overcome these limitations. These include modifying the asymmetry approach, where instead of taking a reference from the upfield part of the z-spectrum, frequencies adjacent to the APT frequency in the downfield region are used (Li et al., 2015; Zhou et al., 2013; Zaiss et al., 2013).

More complex model-based approaches have also been developed using Bloch-McConnell and Lorentzian-based approaches (Ray et al., 2016; Jones et al., 2011a) though such metrics have largely only been applied in non-human preclinical studies, or at high field strengths (7 T) that are, as yet, not routinely available in a clinical context. Where a model-based approach has been tested on data derived from clinically acute stroke patients (Tee et al., 2014), the model developed to isolate the APT metric used 3 pools to model water, APT, and semisolid MT + NOE contributions. However, the combination of magnetisation transfer and NOE effects within a single pool might feasibly have introduced bias into the measures of, or reduced sensitivity to, changes in the APT effect, and as such might not be modelled well within a single pool. Feasibly, a separation of the semisolid and NOE effects as two independent pools might be more accurate based on recent clinical literature (Jin et al., 2013; Zhou et al., 2013).

Given the potential of APT imaging to complement existing imaging techniques to provide clinically-relevant information, there is a need to develop analysis techniques that deliver a robust and repeatable APT metric. Both model-free and model-based solutions exist. Hence, the objectives of this work were: firstly, to determine whether substantial differences are observed between 3- and 4-pool model-based analysis of APT CEST in acute stroke; and secondly, to compare model-based and model-free quantification techniques for CEST imaging that specifically separate APT and NOE effects for application in the clinical setting. Towards this end, a methodological comparison of different CEST quantification techniques was undertaken using imaging data from healthy volunteers and a cohort of acute stroke patients.

1.1. Theory

A wide range of quantification techniques has been proposed which, to varying extents, try to deal with competing magnetisation transfer effects and produce purely APT-weighted contrast. The model-free and model-based quantification techniques compared in this study are detailed in Tables 1 and 2. A brief description of each technique is presented below.

Table 1

Model-free APT quantification techniques. $S(\omega)$ is the sampled signal spectrum interpolated onto the ω frequency axis. S_0 is the unsaturated acquisition.

Model-free technique	General form	Parameters	References
MTR_{asym}(3.5 ppm)	$\frac{S(-\omega_1) - S(\omega_1)}{S_0}$	$\omega_1 = 3.5$ ppm	Zhou et al. (2003)
APT^*	$\left[\frac{S(\omega_1) + S(\omega_2)}{2} - S(\omega_3)\right] \cdot \frac{1}{S_0}$	$\omega_1 = 2.9$ ppm $\omega_2 = 4.1$ ppm $\omega_3 = 3.5$ ppm	Jin et al. (2013)
MTR_{Rex}(APT)	$\left[\frac{1}{S(\omega_3)} - \frac{2}{S(\omega_1) + S(\omega_2)}\right] \cdot S_0$	$\omega_1 = 2.9$ ppm $\omega_2 = 4.1$ ppm $\omega_3 = 3.5$ ppm	Li et al. (2015), Zaiss et al. (2014), Zaiss and Bachert (2013a, 2013b)

1.1.1. Model-free quantification techniques

The model-free quantification techniques compared in this study are classical asymmetry analysis, local linear approximation, and spillover-corrected MTR

1.1.1.1. Asymmetry analysis (MTR_{asym}).
The first studies that investigated APT effects did so using a simple measure of spectral asymmetry, MTR_{asym}, which inherently captures changes on both sides of the z-spectrum together, and in this case it thus relies on one side being constant in the face of any change in APT (such as pH effects). It has become evident that APT asymmetry can be strongly diluted in the presence of competing saturation effects in pathology such as ischaemia (Li et al., 2015). The conceptual and computational simplicity of MTR_{asym} means it continues to be widely used for measuring CEST effects (Zhou et al., 2013; Zaiss et al., 2013; Paech et al., 2014).

1.1.1.2. Local linear approximation technique (APT^*).
Larger B_0 fields result in larger-amplitude CEST effects due to proportionality with water T_1. Wider spectral separation associated with larger B_0 also allows more accurate delineation of the spectral boundaries of the APT peak. Jin et al. (2013) developed a quantification technique, used at 9.4 T, that identified upper and lower frequency boundaries for the APT peak. A line segment connecting the two points gave a linear approximation to non-APT effects over that narrow spectral range (*i.e.* a local linear approximation), with the midpoint corresponding to the location of the APT peak maximum, against which the APT effect observed in the data at 3.5 ppm could be calculated. The APT^* technique can be considered as an extreme simplification of z-spectrum fitting where all effects apart from APT are locally linearly approximated.

1.1.1.3. Spillover-corrected MTR (MTR_{Rex}).
MTR_{Rex} is similar in form to the APT^* measure, the difference being that it inverts the z-spectrum in order to analytically eliminate relaxation terms arising from direct water saturation (RF spillover) and semisolid MT (Zaiss et al., 2014), yielding a less contaminated measure of APT.

1.1.2. Model-based quantification techniques

The model-based techniques used in this study are Lorentzian difference analysis and multi-pool modelling

1.1.2.1. Lorentzian difference analysis (LDA).
The conventional LDA technique is based on steady-state saturation of tissue with low-amplitude RF pulses. This minimises the broadband CEST effects from semisolid tissue, and the resulting z-spectrum can be described as simply a combination of direct water saturation (a Lorentzian line shape whose parameters are estimated from the data), and the solute pools of interest (Jones et al., 2012). Thus, subtracting a fitted Lorentzian from the acquired CEST data removes direct water saturation and what remains are residuals that reveal the other exchange effects and directly quantify saturation of the solute pools.

Table 2

Model-based APT quantification techniques. $S(\omega)$ is the sampled signal spectrum interpolated onto the ω frequency axis. S_0 is the unsaturated acquisition. $S_{(pools)}{}^{model}$ is the signal spectrum obtained through model fitting, the subscript $(pools)$ refers to the exchange pool for which the model fit is obtained.

Model-based technique	General form	Parameters	References
$APTR_{paLDA}$	$\int_{\omega_1}^{\omega_2} \frac{S_{(pools)}^{model}(\omega) - S^{raw}(\omega)}{S_0^{model}} d\omega$	$\omega_1 = 3.0$ ppm $\omega_2 = 4.0$ ppm $pools := water\ \&\ semisolid$	Based on (Jones et al., 2011a; Jones et al., 2012; Jones et al., 2013; Jones et al., 2011b)
$Multi - pool\ APTR^*$	$\frac{S_{water}^{model}(\omega_1) - S_{(pools)}^{model}(\omega_1)}{S_0^{model}}$	$\omega_1 = 3.5$ ppm $pools : water\ \&\ amide$	Tee et al. (2014), Chappell et al. (2013), Tee et al. (2015)

At 7 T, a range of different z-spectral effects were observed across the whole of the spectrum that could be associated with both chemical exchange and relayed transfer effects.

1.1.2.2. Multi-pool model fitting (APTR).* Multi-pool model fitting is distinct from the aforementioned quantification techniques in that the fitted z-spectra are generated from a set of model parameters that directly describe the underlying physical parameters, such as exchange rate, relaxation times, and metabolite concentrations. Magnetisation exchange interactions between bulk water and different metabolites are described by separate exchange pools, with each pool transferring saturation to the main water pool on which a signal accumulates. Each pool is described by a set of Bloch Equations coupled together through mass-conserving exchange rates. Model fitting can be performed using a least-squares or Bayesian approach. Bayesian fitting in particular allows the use of parameter priors that are relevant for *in-vivo* data where knowledge of the statistical distribution of tissue parameter values can be incorporated. There is a risk of over-fitting and the fitting process is computationally expensive. The advantage of model fitting is that it allows the spectral contributions of different species to be isolated by subtracting unwanted saturation components from the pools of interest. This has been exploited previously to define the APTR* metric (Tee et al., 2014; Harston et al., 2015). After fitting multiple pools to the spectral data, only a subset are simulated to predict the effect arising from a single pool, or a combination thereof. The apparent APT ratio, APTR*, is obtained by simulating the combined amide and bulk water pools, ignoring any other pools included in the fit to the original z-spectral data, and comparing this to a simulation of only the water pool. APTR* is then the difference between the two predictions at 3.5 ppm.

In our previous study (Tee et al., 2014) where we compared a range of APT quantification metrics at 3 T, this model-based approach to APT quantification was found to be more repeatable and robust than asymmetry measures. The model-based technique was subsequently used in the clinical study of ref. (Harston et al., 2015). In principle, the model-based quantification approach used was less sensitive to downfield NOE effects than asymmetry.

The 3-pool model used in this study comprises a bulk water pool, an amide pool, and a third pool that attempts to account for both semisolid and NOE effects. The third pool, thus, groups together saturation effects from NOE and semisolid MT exchanges without distinguishing between these two signal sources. This may be sub-optimal given the observed differences in the line shape of semisolid MT and the region over which NOE effects have been observed. The 4-pool model used in this study extends the model such that semisolid MT and NOE exchanges are described as follows: a pool that models semisolid MT as a classic Lorentzian effect centred at the water resonance, and pool that models NOEs, with a resonance frequency downfield of water based on observations in the literature. This was done with the aim of achieving a better separation of CEST effects.

2. Methods

2.1. Study details

Six healthy volunteers (median age: 34 years) were recruited and imaged under an agreed technical development protocol approved by the institution's Research Governance Office. These volunteers underwent imaging with four repeated CEST scans at three separate time points (initial, at 24 h and at 1 week).

Eighteen patients presenting with acute ischaemic stroke were recruited into a prospective observational imaging study according to research protocols agreed by the UK National Research Ethics Service Committee (references 12/SC/0292 and 13/SC/0362) as previously described (Harston et al., 2015). After exclusions on the grounds of motion corruption, imaging artefacts, and secondary heamorrhage, this left 12 datasets for analysis as described in the original study. The median time from onset was 2 h 59 min, 58% female, with a median patient age of 79.5 years, and a median NIHSS score at presentation of 11. Individual patient demographics are detailed in ref. (Harston et al., 2015).

2.2. Image acquisition

All patient scans were performed on a 3 T Siemens Verio scanner using a 32-channel head coil. Each patient underwent a T_1-weighted MP-RAGE structural scan (voxel dimensions $1.8 \times 1.8 \times 1.0$ mm^3, FOV = 228 mm, TR = 2040 ms, TE = 4.55 ms, T1 = 900 ms), diffusion-weighted imaging (DWI) in three directions ($b = 0$, $b = 1000$ s/mm^2), multiple post-labelling delay vessel-encoded pseudo-continuous arterial spin labelling perfusion-weighted imaging (Okell et al., 2013), and single-slice CEST imaging with voxel dimensions $3 \times 3 \times 5$ mm^3. The single-slice CEST imaging plane was localised by a clinician based on the DWI lesion at the time of scanning. Pulsed CEST preparation was performed with 50 Gaussian pulses at a flip angle of 184° and a 50% duty cycle (each pulse 20 ms duration, with 20 ms inter-pulse delay) to achieve an average B_1 power of 0.55 μT. Crusher gradients were applied between pulses to spoil the residual transverse magnetisation. A spin echo echo planar imaging readout (TR = 5 s, TE = 23 ms, 64×64 matrix size, 6/8 partial Fourier) was performed after the CEST preparation pulses. An evenly distributed sampling (EDS) scheme was used up to Patient 4, where 32 saturation frequencies were used from -4.5 ppm to 4.5 ppm in steps of 0.3 ppm, and 300 ppm. For Patient 5 to Patient 12 (and all the healthy volunteers), a semi-optimal sampling scheme (semi-OSS) that had a higher density of points around the amide resonance frequency was used (-300, -50, -30, -4.1, -3.8, -3.5, -3.2, -2.9, -0.9, -0.6, -0.3, 0.0, 0.3, 0.6, 0.9, 2.9, 3.1, 3.2, 3.3, 3.4, 3.4, 3.5, 3.5, 3.6, 3.6, 3.7, 3.8, 3.9, 4.1, 30, 50, 300 ppm) (Harston et al., 2015; Tee et al., 2013). Data The total acquisition time for the CEST sequence was 2 min 45 s. A DWI (at 24 h) and/or T_2-weighted FLAIR (at 1 week) follow-up scan to enable the definition of tissue outcome was taken.

Table 3
Four-pool model priors expressed as a mean and standard deviation (SD). Tabulated values are those used for the clinical data. For 3-pool model priors refer to ref. (Tee et al., 2014).

Parameter	Water (Tee et al., 2014)		APT (Tee et al., 2014)		Symmetric semisolid		NOE	
	Mean	SD	Mean	SD	Mean	SD[a]	Mean	SD[a]
M_0 (norm.)	0	1×10^6	$\frac{90\text{ mM}}{112\text{ M}}$	$\frac{20\text{ mM}}{112\text{ M}}$	0^a	1×10^6	0^a	1×10^6
k_{ex} (Hz)	–	–	20	$e^{1.0}$	60^b	$e^{1.0}$	20^c	$e^{1.0}$
T_1 (s)	1.3	0.15	0.77	0.15	1.0 (Tee et al., 2014; Liu et al., 2013)	0.15	0.77^c	0.15
T_2 (ms)	70	14	10	2	0.1^b	0.02	0.3 (Liu et al., 2013)	0.06
$\Delta\omega$ (ppm)	0	$\sqrt{0.1}$	3.5	1×10^{-6}	0 (Liu et al., 2013)	1×10^{-6}	-3.5 (Liu et al., 2013)	1×10^{-6}

Glossary – M_0: pool concentration relative to water pool (water pool M_0 is absolute), k_{ex}: pool→bulk water exchange rate, T_1: longitudinal relaxation time, T_2: transverse relaxation time, $\Delta\omega$: chemical shift with respect to water pool.
[a] Same value from 3-pool model was used (Tee et al., 2014).
[b] Based on 4-pool model in ref. (Liu et al., 2013).
[c] Same value as APT pool was used (Liu et al., 2013).

2.3. Processing

Image processing and analysis was performed using the FMRIB Software Library (FSL) (Smith et al., 2004; Jenkinson et al., 2012) and MATLAB (Mathworks, Inc., Natick, MA).

2.3.1. Image processing

The Brain Extraction Tool in the FSL package (Smith, 2002) was used to remove the skull and non-brain areas in all of the collected data. All of the imaging modalities were transferred to the structural space, and within time point image registration was performed using FMRIB's Linear Image Registration Tool (FLIRT). Across time point image registration was done using FMRIB's Non-linear Image Registration Tool (FNIRT) for patients, and FLIRT for healthy subjects, both available in the FSL package (Jenkinson et al., 2012; Jenkinson et al., 2002; Jenkinson and Smith, 2001). The different CEST frequency offsets were motion-corrected using linear co-registration to the unsaturated acquisition. The quantified APT effects using the different metrics were transformed to the structural space using rigid body transformation estimated using FLIRT. The T_1 structural data were segmented using FMRIB's Automated Segmentation Tool (FAST) into cerebrospinal fluid (CSF), grey and white matter (GM and WM).

2.3.2. Region of interest (ROI) definitions in native space

In healthy subjects, the ROIs used were a whole slice mask, a grey matter mask, and a white matter mask, defined as follows. Grey matter and white matter masks were first generated from partial volume (PV) estimates using the FSL tool FAST (Zhang et al., 2001) on the presenting T_1-weighted scan and the images were transformed to the resolution of the CEST images. Thresholds were applied to create healthy subject masks in the data space:

- Whole slice mask: PV threshold of 50% applied to the GM PVE map.
- GM mask: voxels with a GM PV threshold of 70%.
- WM mask: voxels with a WM PV threshold of 90%.

In stroke patients, infarct at presentation was defined using semi-automated delineation of ADC below an externally validated threshold of 620×10^{-6} mm^2/s (Purushotham et al., 2015). Final infarct was defined preferentially on the 1 week FLAIR image, or, if not available, the $b = 1000$ DWI at 24 h (Harston et al., 2017). The mask representing perfusion deficit was generated using a threshold approach where voxels with a cerebral blood flow (CBF) threshold of less than 20 ml/100g/min were identified and clustered, and then used as a guide for manual delineation by an expert clinician (Harston et al., 2015). The ROIs used in this study were:

- Ischaemic core: within both presenting and final infarct definitions.

- Infarct growth: within the final infarct, but not within the presenting infarct.
- Oligaemia: tissue present in the perfusion deficit but not the final infarct.
- Mirrored contralateral mask: contralateral ROIs were obtained by non-linearly registering the pathological masks to standard MNI152 space, reflection in the sagittal plane, and transforming back to CEST space.

These ROI definitions are in keeping with those used in ref. (Harston et al., 2015) but have been updated to improve ROI fidelity with tissue fate (Harston et al., 2017).

2.3.3. Model fitting

A continuous-wave approximation of the multi-pool Bloch-McConnell model, including both 3 and 4 pools as described in Theory, was fitted to the data (Chappell et al., 2013; Tee et al., 2012; Chappell et al., 2011) using the implementation in the FSL tool BayCEST, which uses the variational Bayes FABBER model-fitting routine (Tee et al., 2014; Chappell et al., 2013; Chappell et al., 2009). The parameter prior distributions are listed in Table 3. The CEST data were compensated for B_0 inhomogeneity *via* a variable in the model-fitting algorithm that accounted for water resonance shift. The B_0 map obtained from the 4-pool model was used to correct the techniques listed in Table 1 by voxel-wise interpolation of the acquired spectra. The model-based metrics are implemented in *Quantiphyse*, made available for download at www.quantiphyse.org (Croal et al., 2018).

2.3.4. Post-acquisition LDA (paLDA)

In this retrospective study it was not possible to follow the acquisition methodology from the original LDA approach. Instead, a post-acquisition LDA technique was used where, rather than applying an ultra-low B_1 during the acquisition phase, the data acquired using a conventional CEST scheme were used and only the data points that were expected to exclude APT and NOEs were used for model fitting within the BayCEST algorithm (Tee et al., 2014). The data points at ± 300 ppm, ± 50 ppm, ± 30 ppm, ± 0.6 ppm, ± 0.3 ppm, and 0 ppm, were assumed to exhibit contribution from the bulk water and semisolid MT pools only and were fitted to a 2-pool model comprising water and semisolid MT. Subtraction of the acquired *z*-spectrum (B_0-corrected) from the fitted spectra yielded a residual corresponding to the APT effect. A final value at each voxel was obtained by integrating the residual between 3.0 to 4.0 ppm (in increments of 0.01 ppm) using trapezoidal integration. A study by ref. (Heo et al., 2016a) used a similar approach but where offset frequencies from only one side of the *z*-spectrum were used (EMR technique), exhibiting contrast in a human glioma study at 3 T (Heo et al., 2016a, 2016b).

2.4. Analysis

The analysis plan was first to define the reproducibility and contrast characteristics of healthy and pathological tissues. The optimal image analysis approach as defined by these metrics was then evaluated across pathological tissue types. All analyses were done in the native space of the data.

2.4.1. Repeatability analysis

The repeatability of each technique between time points and between individuals was assessed separately in healthy subjects and in patient contralateral tissue. Repeatability was quantified using the coefficient of variation (CoV, standard deviation divided by the mean).

2.4.2. Spatial variability

Spatial variability (CoV within an ROI) was used as a measure of an ROI's spatial heterogeneity and was found in healthy subjects and patient contralateral tissue.

2.4.3. Grey versus white matter APT signal

The difference in the mean APT signal between grey and white matter was expressed as a percentage relative to the grey matter signal mean.

2.4.4. Contrast-to-noise ratio (CNR)

CNR was defined as follows: pathological ROI contrast using a given technique was defined as the difference in mean signal between the ROI (m_{ROI}) and contralateral (m_{CO}) tissue, and noise was defined as the standard deviation (SD) in the contralateral hemisphere (SD_{CO}): $CNR = (m_{ROI} - m_{CO})/SD_{CO}$.

2.4.5. Comparison of the optimum technique in patients

The optimal technique was chosen according to the best performance across repeatability, spatial variability, and CNR. For pooled analysis across tissue types, data were normalised to their mean in the contralateral hemisphere to produce a relative measure. This accounted for systematic variability between individuals not already controlled for by the quantification technique. The contralateral-normalised individual patient means were weighted by the number of contributing voxels and pooled to give a voxel-weighted group mean for each tissue outcome.

2.4.6. Statistical analysis

Appropriate statistical tests were used including: two-tailed paired t-test; comparisons between multiple groups (ROIs and/or quantification techniques) were preceded with a one-way ANOVA test for significance; and, post-hoc pairwise testing was done using the Tukey-Kramer method with $\alpha_{crit} = 0.05$. The number of degrees of freedom (DOF) used in the statistical tests was based on the number of patients.

3. Results

Images from representative patients are shown in Fig. 1 for each of the six quantification techniques.

3.1. Repeatability analysis

None of the measures exhibited significant variation between healthy subjects or between time points, except for the 4-pool technique (significant interaction), and the paLDA technique (significant interaction and time point variability). Repeatability between subjects is shown in Fig. 2a. The model-based techniques had the lowest CoV.

Four-pool APTR* had the lowest CoV in both healthy subjects and patient contralateral tissue (3.16%, 5.34%). This was followed by the paLDA technique (4.22% in healthy subjects), and 3-pool APTR* (4.63%). Using classical asymmetry, the healthy subject CoV was
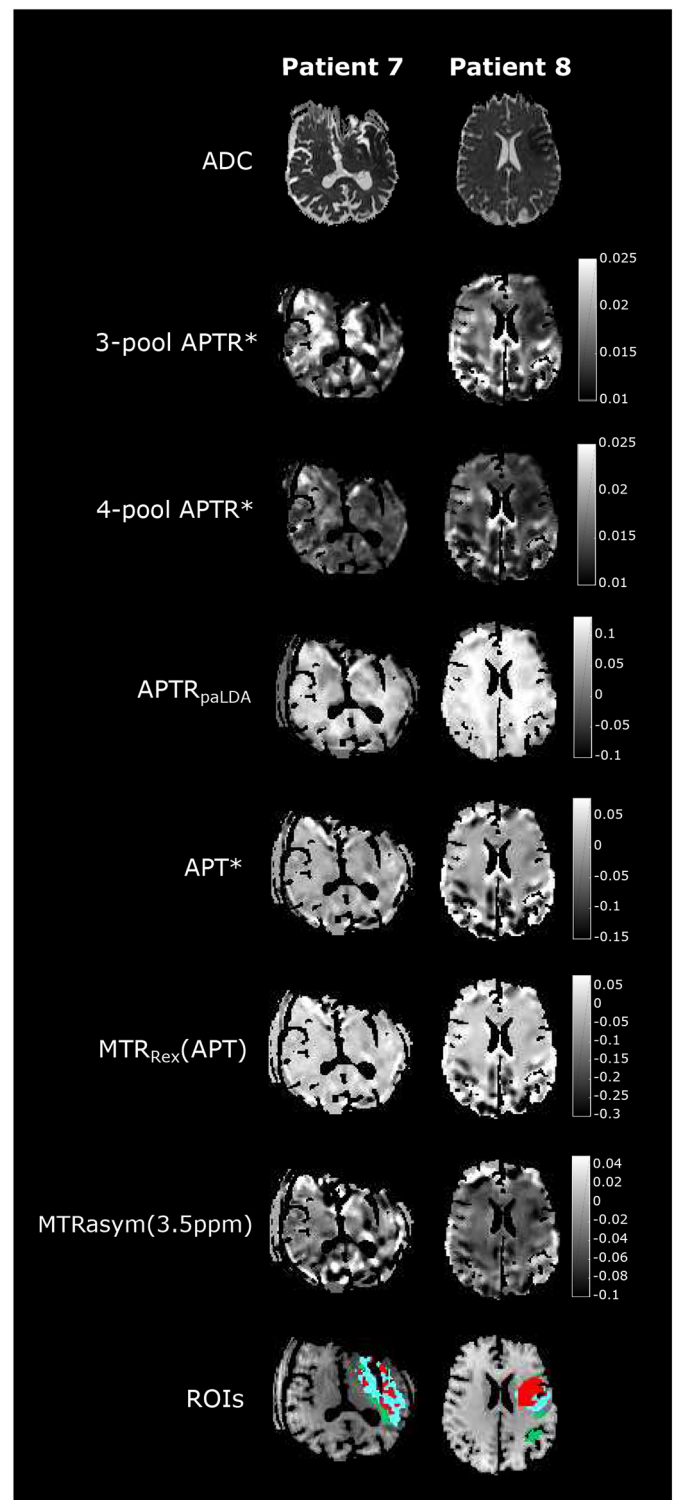

Fig. 1. Images from representative patients, showing (from left): presenting ADC image, slices from each of the six quantification techniques, and the ROIs overlaid on a T_1 image. Red: ischaemic core, green: oligaemia, and cyan: infarct growth.

9.45%.

3.2. Spatial variability

The spatial variability of each technique in healthy subjects and patient contralateral tissue is shown in Fig. 2b. Model-based APT

Subject repeatability

(a)

Spatial variability

(b)
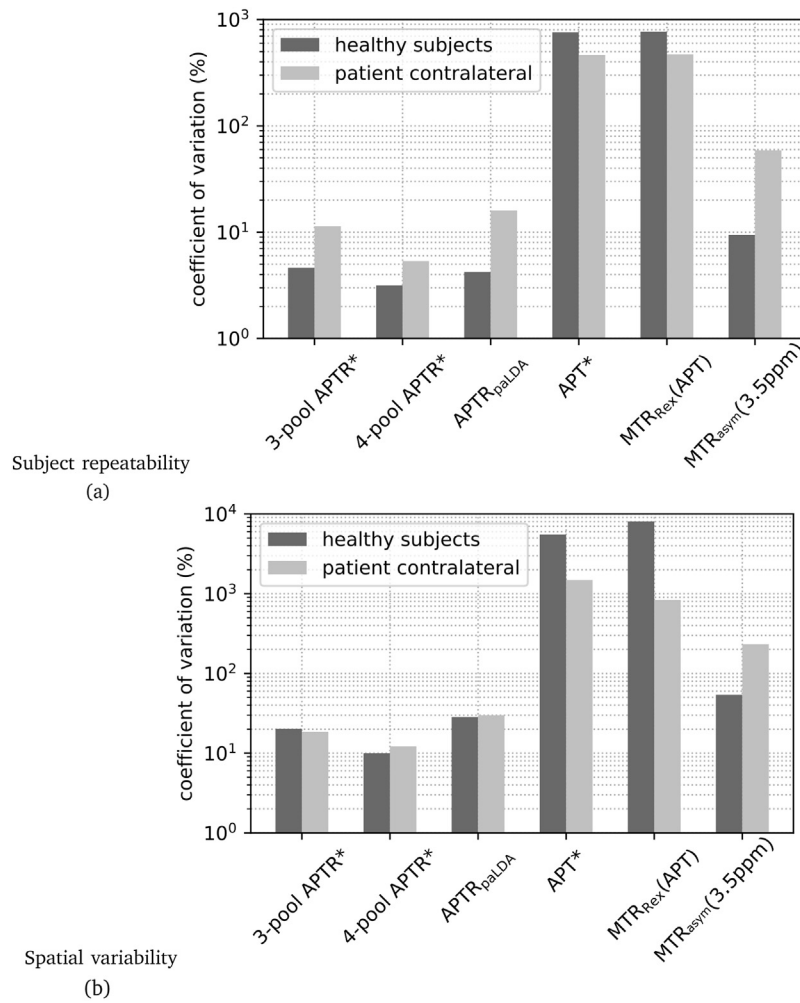
Fig. 2. (a) Subject repeatability of the APT signal in healthy subjects and patient contralateral tissue using different techniques, (b) spatial variability of APT measures in healthy subjects and patient contralateral tissue using different quantification techniques.

measures exhibited lower spatial variability than the model-free techniques. Four-pool APTR* had the lowest spatial variability (10.0% in healthy subjects), followed by 3-pool APTR* (20.17%) and APTR_{paLDA} (28.4%).

3.3. Grey versus white matter APT signal

Contrast between grey and white matter in healthy subjects when analysed using the various APT quantification techniques examined here is shown in Fig. 2. The multi-pool techniques exhibited the smallest difference between grey and white matter; 4-pool APTR* contrast was 1.88%, and contrast was 2.48% using 3 pools. The remaining techniques exhibited contrast of at least 30%. Model-free techniques had the highest contrast between grey and white matter.

3.4. Ischaemic core CNR

Ischaemic core CNR is shown for the different techniques in Fig. 3. Four-pool APTR* exhibited the highest CNR (0.74). Three-pool APTR* had a CNR of 0.55, and APTR_{paLDA} had a CNR of 0.37. Three- and 4-pool APTR* exhibited similar absolute contrast (0.0024, 0.0019), but 3-pool APTR* had the lower CNR owing to a larger noise term (a contralateral SD of 0.0035 v.s. 0.0021) compared to the 4-pool model. The paLDA technique exhibited larger absolute contrast (0.0034) but this was dominated by a noise term which was approximately an order of magnitude larger (0.03) than the 3-pool measure. The APT* technique
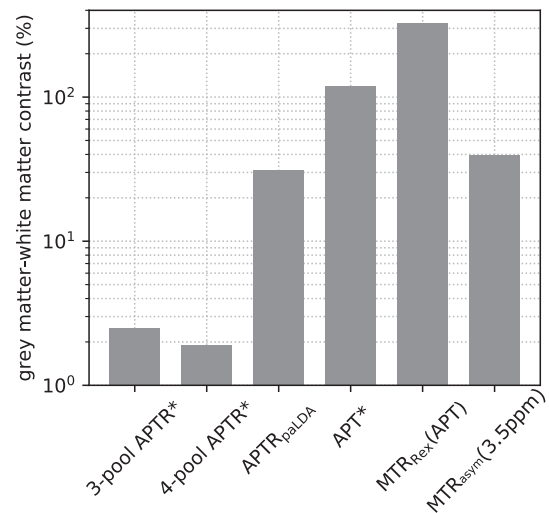
Fig. 3. Contrast between grey and white matter in healthy subjects using different techniques for quantifying APTR.
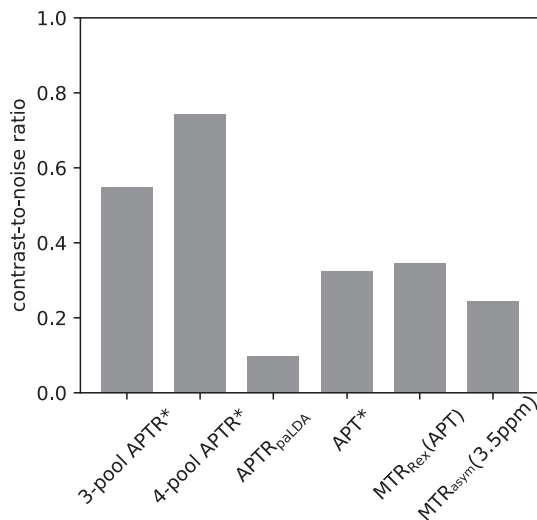
Fig. 4. Ischaemic core CNR using different APT quantification techniques.

and MTR_{Rex} exhibited a similar CNR (0.36).

3.5. Choice of optimal technique

Based on all four groups of analyses presented above, the multi-pool models performed best across all of the metrics, and so, proceed on for further analyses.

3.6. Effects of adding a fourth pool to multi-pool analysis

The relative (to contralateral tissue) mean $APTR^*$ in patients is presented in Fig. 4. Within the grey matter mask, there was significant differentiation between the ROIs using both 3-pool and 4-pool analysis. In white matter voxels, however, there was no significant differentiation between ROIs.

In terms of the pattern of contrast, in grey matter the 3-pool and 4-pool ischaemic core signals were significantly different from oligaemic tissue. In the ischaemic core, 3-pool relative $APTR^*$ was nearly identical to the 4 pool measure (0.87 ± 0.09 v.s. 0.87 ± 0.07); likewise in oligaemic tissue (relative $APTR^*$ 1.03 ± 0.15 using 3 pools, and 1.01 ± 0.10 using 4 pools). In the whole slice, infarct growth tissue exhibited an intermediate value using 3-pool analysis (relative mean: 0.95 ± 0.04) that put it approximately mid-way between ischaemic core and oligaemic relative $APTR^*$, corresponding to an infarct growth CNR of 0.23. This contrast of the the infarct growth ROI signal was reduced, CNR = 0.08, using 4-pool analysis as the relative mean within the infarct growth ROI included unity (0.98 ± 0.04).

4. Discussion

4.1. Choice of optimal technique

Robustness analysis of the six quantification techniques indicated that the multi-pool model-based technique had the smallest contrast between grey and white matter, whereas model-free techniques exhibited the highest contrast. Model-based techniques were the most repeatable across time points and between subjects, the lowest CoV being achieved using 4-pool $APTR^*$, followed by 3-pool $APTR^*$ and paLDA. Model-based techniques also exhibited the lowest spatial variability, of which 4-pool $APTR^*$ was by far the most uniform, followed by 3 pools and paLDA. Four-pool analysis yielded the highest ischaemic core CNR, followed by the 3-pool technique.

Requirements of a technique in a clinical imaging context are that it is repeatable and maximises ischaemic core contrast. In these respects,

4-pool $APTR^*$ was the optimal technique. Model-based techniques, multi-pool in particular, were more robust than model-free techniques. Similar $APTR^*$ in grey and white matter was expected on the basis of uniform brain tissue pH; however, it is not known whether chemical properties of amides, such as concentration and exchange rate, ought to be the same in grey and white matter. $APTR^*$ has shown minimal tissue contrast (Fig. 2), and similar patterns of change in response to ischaemia.

In the original APT^* study by Jin et al. (2013), the APT^* technique demonstrated good detection sensitivity at 9.4 T. In the present clinical study, a relatively widely-available 3 T field was used, rather than a more exotic ultra-high-field strength, making it difficult to accurately identify the spectral boundaries of the solute pools. This is compounded by the use of pulsed, *versus* continuous-wave, CEST schemes that are necessary to limit tissue heating within clinical safety bounds at the expense of being less frequency-selective. It is also necessary to have sufficient sampling points at the boundaries, and at the peak, for them to be accurately located. Higher saturation powers also broaden the CEST peaks, which reduces the accuracy of quantification using this technique.

The inverse z-spectrum analysis technique, MTR_{Rex}, is designed to remove direct water saturation and semisolid MT effects. However, $MTR_{Rex}(APT)$ exhibited the highest grey-white matter contrast, where water relaxation times and semisolid MT concentrations are significantly different. This is likely because the conditions under which MTR_{Rex} was evaluated deviate from three assumptions made in its derivation. Firstly, at 3 T, the NOE pool exhibits a non-negligible tail of saturation that overlaps with downfield APT (Zaiss et al., 2016). This causes the APT MTR_{Rex} label scan at 3.5 ppm (Z_{lab}) to be contaminated by non-zero exchange-dependent relaxation terms from aromatic NOE-related protons, meaning MTR_{Rex} is no longer selective for APT-only saturation. NOEs, associated with lipids, may be imparting the grey matter-white matter contrast to the MTR_{Rex} APT measure. However, reference images (Z_{ref}) at -3.5 ppm for CEST metrics can be generated from Bloch equation fitting or Lorentzian fitting by taking only MT data (water + semisolid MT) far from the water signal, such as beyond $\pm$ 10 ppm. Secondly, in the original MTR_{Rex} study by Zaiss et al. (Zaiss and Bachert, 2013a), it was assumed that $B_1 >> k_{amide}$ (in particular, B_1 at least $10 \times k_{amide}$). In the present study, however, a relatively low B_1 of 0.55 μT was used, where the former assumption holds only weakly (B_1 approx. $5 \times k_{amide}$). Finally, the dependence of MTR_{Rex} on inverse analysis means that its usage is limited in cases where spectral resolution is relatively low such as at 3 T (or in the presence of large direct water saturation and semisolid MT effects due to $B_1 >> 1 \mu T$), where the inversion can break down close to 0 ppm (Heo et al., 2017; Wang et al., 2017). With respect to the paLDA technique, the Lorentzian difference signal was small at 3 T compared to the study at 7 T using conventional LDA in ref. (Jones et al., 2012). Thus, the present study was limited to evaluating these techniques in sub-optimal conditions, and different results might have been found for an equivalent high-field preclinical CEST study.

4.2. Effects of adding a fourth pool to multi-pool analysis

In assessing the effects of adding a fourth pool to multi-pool modelling of APT, neither 3- nor 4-pool $APTR^*$ varied significantly between healthy subjects or time points, and both exhibited a decreased ischaemic core signal with respect to healthy subjects and patient contralateral tissue which was significantly different from oligaemic tissue. In healthy subjects, the 4-pool model had lower contrast between grey and white matter, and was the most repeatable technique between subjects and across time points. Four-pool analysis also exhibited lower spatial variability and yielded a higher ischaemic core CNR.

The improvements offered by the 4-pool model appear be accompanied by reduced contrast between infarct growth tissue and normal
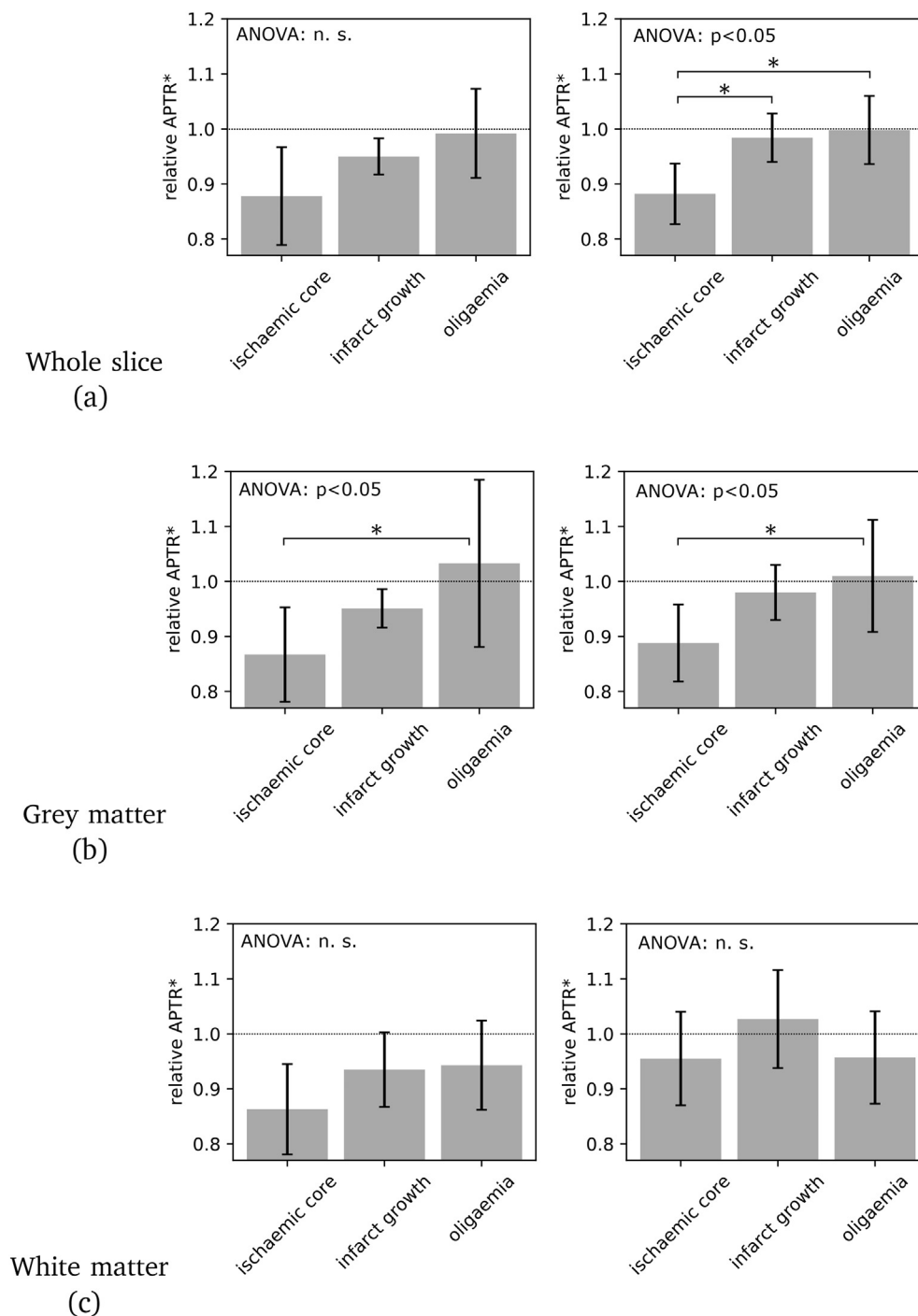
Fig. 5. Multi-pool relative APTR* within different ROIs using 3-pool (left column) and 4-pool (right column) analysis in (a) the whole slice, (b) grey matter voxels, and (c) white matter voxels. Error bars are the 95% CI. Significance between ROIs is denoted by an asterisk.

tissue. Three-pool analysis yielded an intermediate infarct growth APTR*, appearing to exhibit gradation in APTR* as a function of tissue outcome, offering the potential to use the metric to identify 'tissue at risk', *i.e.* tissue that is viable according to diffusion measures on presentation, but that does go on to infarct. This pattern was not observed using 4-pool analysis where contrast was largely confined to the ischaemic core. Since this reduction in contrast was the result of separately modelling NOEs and semisolid effects (hence decoupling the effects of NOEs from other metabolite peaks), it suggests that the origin of infarct growth contrast might be associated with NOEs, and, therefore, the changes in NOEs in acute stroke need to be examined further. In white matter voxels, 3-pool analysis retained a decreased ischaemic

core signal, whereas when using 4-pool analysis the ischaemic core signal was closer to unity. Spatial variability of the ischaemic core signal in white matter was also higher using 3-pool analysis compared to 4 pools. NOEs have been shown to exhibit statistically significant change in stroke (Msayib et al., 2017) and to be more strongly associated with white matter compared to grey matter (Jin et al., 2013; Jones et al., 2011a; Zhang et al., 2016). This all implies that the reduction in infarct growth contrast using 4 pools represents a trade-off between identifying tissue to target for treatment and biophysically more accurate modelling of CEST effects. The 3-pool model-based analysis, whilst less biophysically accurate, may still be useful for identifying penumbra, not purely because of gradation in APT effects,
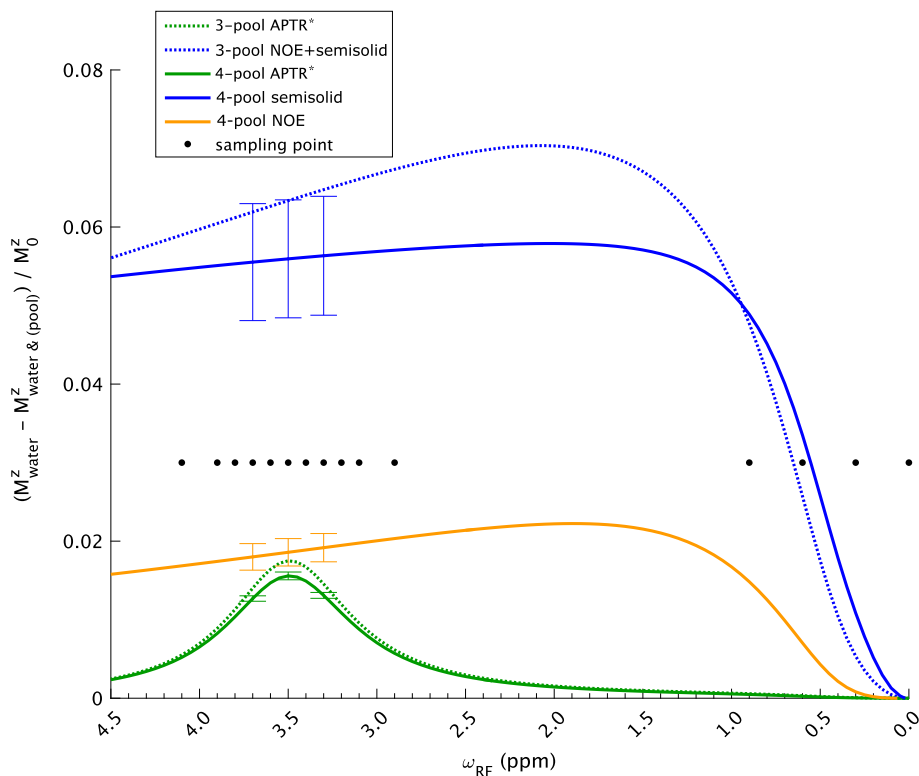
Fig. 6. Simulated spectrum of healthy subject data. Dotted lines are the 3-pool spectra and solid lines are the 4-pool spectra. Sample points used in model fitting are indicated by black dots. Error bars indicate the SD across simulations at representative points.

for example associated with changes in pH, but also by incorporating a degree of changes associated with NOEs.

In multi-pool models, exchange pools are distinct from one another in that direct transfer of magnetisation only occurs with the bulk water pool. However, broad spectral phenomena such as semisolid effects can overlap with peaks from other pools and may therefore indirectly influence the distribution of saturation between pools. Asymmetry in the z-spectrum upfield of water has been attributed NOEs (Zhou et al., 2013). Since NOEs can account for spectral asymmetry, it allows semisolid effects to be described as a symmetric phenomenon centred at the water resonance (Zaiss and Bachert, 2013b).

In order to explore the way in which addition of the NOE pool affected quantification of the downfield APT signal, the model-fitted spectra averaged over healthy subjects are presented in Fig. 5. In the 3-pool model, the line shapes downfield of water are 3-pool NOE +semisolid effects (dotted blue), representing combined NOEs and an asymmetric semisolid pool, and 3-pool APTR* (dotted green). A fourth pool is added to separately model NOEs (4-pool NOE, orange) and a symmetric semisolid pool (solid blue). The semisolid pool line shape described a similar profile to 3-pool NOE (solid blue v.s. dotted blue). The main difference was that the 4-pool NOE line shape, owing to a longer T_2, was narrower than the 3-pool NOE line shape, and exhibited a weaker tail of saturation overlapping with the APT peak. This led to a lesser degree of coupling between upfield and downfield spectra. The downfield NOE tail phenomenon has also been recently observed though water exchange (WEX) spectroscopy of BSA phantoms as well as higher-field healthy subject studies (Liu et al., 2013; Zaiss et al., 2016).

Increasing the number pools, and therefore the number of model parameters, can lead to overfitting or fitting to noise that would result in higher spatial variation. However, in this case, adding a fourth pool yielded more repeatable APTR* in healthy subjects, which also exhibited lower spatial variability compared to 3-pool APTR*. This is more consistent with the expectation that APT would be uniform across healthy subjects and within a given subject, and supports the

appropriateness of using a 4-pool model for the analysis of APT CEST data at 3 T.

Even using 4 pools is still very much an approximation to the many processes going on in the spectrum (Jones et al., 2012). For example, pH-dependent amine resonances are reported around 1.8–1.9 ppm (Haris et al., 2012; Desmond et al., 2014) but their close proximity to the water resonance makes them difficult to detect in a clinical setting. In light of this, adding further pools increases the risk of over-fitting and is hard to justify on clinical data, considering field strength, number of samples, and patient motion.

The effects of amide proton pool concentration and exchange rate have very similar effects on the appearance of the z-spectrum which are difficult to isolate in data acquired a single B_1 power. APTR* is a non-rate-specific metric which seeks to explain overall changes driven by any combination of exchange rate and concentration (Chappell et al., 2013), thus enabling detection of an APT effect irrespective of its origin, and is not dissimilar to non-rate-specific metrics reported in this study. Acquiring data at multiple B_1 powers provides a way for separating exchange rate and concentration, explored using multi-pool model fitting in (Chappell et al., 2013) at the expense of longer scan time, and using a dictionary-based approach in (Heo et al., 2019). In the study of ref. (Ray et al., 2016), pH was isolated using APTR* measures, though this relied on acquiring quantitative T_1 maps, and was shown in an *in-vitro* setting employing BSA protein concentration phantoms.

5. Conclusion

The multi-pool measures performed best across the analyses of repeatability, spatial variability, CNR, and GM-WM contrast, and might therefore be more suitable for use in clinical imaging of acute stroke. Addition of a fourth pool that separates NOEs and semisolid effects appeared to be more biophysically accurate and provided better separation of the APT signal compared to the 3-pool equivalent, but this improvement appeared be accompanied by reduced contrast between

infarct growth tissue and normal tissue. As such, the 3-pool model may have more clinical utility in delineating the ischaemic penumbra precisely because it retained some NOE-based contribution. The reduction in contrast between infarct growth tissue and contralateral tissue using 4 pools represents a trade-off between identifying tissue to target for treatment and biophysically more accurate modelling of CEST effects.

Data statement

Acknowledgements

References

Astrup, J., Siesjo, B.K., Symon, L., 1981. Thresholds in cerebral ischemia – the ischemic penumbra. Stroke 12 (6), 723–725.

Chappell, M.A., Groves, A.R., Whitcher, B., Woolrich, M.W., 2009. Variational Bayesian inference for a nonlinear forward model. IEEE Trans. Signal Process. 57 (1), 223–236.

Chappell, M.A., Groves, A.R., MacIntosh, B.J., Donahue, M.J., Jezzard, P., Woolrich, M.W., Apr 2011. Partial volume correction of multiple inversion time arterial spin labeling MRI data. Magn. Reson. Med. 65 (4), 1173–1183.

Chappell, M.A., Donahue, M.J., Tee, Y.K., Khrapitchev, A.A., Sibson, N.R., Jezzard, P., Payne, S.J., Aug 2013. Quantitative Bayesian model-based analysis of amide proton transfer MRI. Magn. Reson. Med. 70 (2), 556–567.

Croal, P.L., Msayib, Y., Ray, K.J., Craig, M., Chappell, M.A., 2018. QuantiCEST: Bayesian model-based analysis of CEST MRI. Proc. Intl. Soc. Mag. Reson. Med.(4803).

Desmond, K.L., Moosvi, F., Stanisz, G.J., May 2014. Mapping of amide, amine, and aliphatic peaks in the CEST spectra of murine xenografts at 7 T. Magn. Reson. Med. 71 (5), 1841–1853.

Haris, M., Nanga, R.P., Singh, A., Cai, K., Kogan, F., Hariharan, H., Reddy, R., Nov 2012. Exchange rates of creatine kinase metabolites: feasibility of imaging creatine by chemical exchange saturation transfer MRI. NMR Biomed. 25 (11), 1305–1309.

Harston, G.W.J., Tee, Y.K., Blockley, N., Okell, T.W., Thandeswaran, S., Shaya, G., Sheerin, F., Cellerini, M., Payne, S., Jezzard, P., Chappell, M., Kennedy, J., Jan 2015. Identifying the ischaemic penumbra using pH-weighted magnetic resonance imaging. Brain 138 (Pt 1), 36–42.

Harston, G.W.J., Minks, D., Sheerin, F., Payne, S.J., Chappell, M., Jezzard, P., Jenkinson, M., Kennedy, J., 2017. Optimizing image registration and infarct definition in stroke research. Ann. Clin. Transl. Neurol. 4 (3), 166–174.

Heo, H.Y., Zhang, Y., Jiang, S., Lee, D.H., Zhou, J., 2016a. Quantitative assessment of amide proton transfer (APT) and nuclear overhauser enhancement (NOE) imaging with extrapolated semisolid magnetization transfer reference (EMR) signals: II. Comparison of three EMR models and application to human brain glioma at 3 tesla. Magn. Reson. Med. 75 (4), 1630–1639 Apr.

Heo, H.Y., Jones, C.K., Hua, J., Yadav, N., Agarwal, S., Zhou, J., van Zijl, P.C., Pillai, J.J., 2016b. Whole-brain amide proton transfer (APT) and nuclear overhauser enhancement (NOE) imaging in glioma patients using low-power steady-state pulsed chemical exchange saturation transfer (CEST) imaging at 7T. J. Magn. Reson. Imaging 44 (1), 41–50 Jul.

Heo, H.Y., Lee, D.H., Zhang, Y., Zhao, X., Jiang, S., Chen, M., Zhou, J., May 2017. Insight into the quantitative metrics of chemical exchange saturation transfer (CEST) imaging. Magn. Reson. Med. 77 (5), 1853–1865.

Heo, H.Y., Han, Z., Jiang, S., Schar, M., van Zijl, P.C.M., Zhou, J., Apr 2019. Quantifying amide proton exchange rate and concentration in chemical exchange saturation transfer imaging of the human brain. Neuroimage 189, 202–213.

Jenkinson, M., Smith, S., Jun 2001. A global optimisation method for robust affine registration of brain images. Med. Image Anal. 5 (2), 143–156.

Jenkinson, M., Bannister, P., Brady, M., Smith, S., Oct 2002. Improved optimization for

the robust and accurate linear registration and motion correction of brain images. Neuroimage 17 (2), 825–841.

Jenkinson, M., Beckmann, C.F., Behrens, T.E., Woolrich, M.W., Smith, S.M., Aug 2012. FSL. Neuroimage 62 (2), 782–790.

Jin, T., Wang, P., Zong, X., Kim, S.G., Mar 2013. MR imaging of the amide-proton transfer effect and the pH-insensitive nuclear overhauser effect at 9.4 T. Magn. Reson. Med. 69 (3), 760–770.

Jones, C.K., Huang, A.J., van Zijl, P.C., 2011a. Exchange-relayed nuclear overhauser effect MRI. Proc. Intl. Soc. Mag. Reson. Med. 19 (2735).

Jones, C., Polders, D., Hua, J., Hoogduin, H., Zhu, H., Zhou, J., van Zijl, P., 2011b. 3D whole brain pulsed CEST acquisition at 7T. Proc. Intl. Soc. Mag. Reson. Med. 19.

Jones, C.K., Polders, D., Hua, J., Zhu, H., Hoogduin, H.J., Zhou, J., Luijten, P., van Zijl, P.C., Jun 2012. In vivo three-dimensional whole-brain pulsed steady-state chemical exchange saturation transfer at 7 T. Magn. Reson. Med. 67 (6), 1579–1589.

Jones, C.K., Huang, A., Xu, J., Edden, R.A., Schar, M., Hua, J., Oskolkov, N., Zaca, D., Zhou, J., McMahon, M.T., Pillai, J.J., van Zijl, P.C., Aug 2013. Nuclear Overhauser enhancement (NOE) imaging in the human brain at 7T. Neuroimage 77, 114–124.

Li, H., Zu, Z., Zaiss, M., Khan, I.S., Singer, R.J., Gochberg, D.F., Bachert, P., Gore, J.C., Xu, J., Feb 2015. Imaging of amide proton transfer and nuclear Overhauser enhancement in ischemic stroke with corrections for competing effects. NMR Biomed. 28 (2), 200–209.

Liu, D., Zhou, J., Xue, R., Zuo, Z., An, J., Wang, D.J., Oct 2013. Quantitative characterization of nuclear overhauser enhancement and amide proton transfer effects in the human brain at 7 tesla. Magn. Reson. Med. 70 (4), 1070–1081.

Msayib, Y., Harston, G.W.J., Ray, K.J., Larkin, J.R., Sutherland, B.A., Sheerin, F., Blockley, N.P., Okell, T.W., Jezzard, P., Baldwin, A., Sibson, N.R., Kennedy, J., Chappell, M., Oct 2017. Downfield CEST signals of the ischaemic core in quantitative imaging of hyperacute stroke, ESMRMB 2017, 34th Annual Scientific Meeting. MAGMA 30 (447).

Okell, T.W., Chappell, M.A., Kelly, M.E., Jezzard, P., Nov 2013. Cerebral blood flow quantification using vessel-encoded arterial spin labeling. J. Cereb. Blood Flow Metab. 33 (11), 1716–1724.

Paech, D., Zaiss, M., Meissner, J.E., Windschuh, J., Wiestler, B., Bachert, P., Neumann, J.O., Kickingereder, P., Schlemmer, H.P., Wick, W., Nagel, A.M., Heiland, S., Ladd, M.E., Bendszus, M., Radbruch, A., 2014. Nuclear overhauser enhancement mediated chemical exchange saturation transfer imaging at 7 tesla in glioblastoma patients. PLoS One 9 (8), e104181.

Purushotham, A., Campbell, B.C., Straka, M., Mlynash, M., Olivot, J.M., Bammer, R., Kemp, S.M., Albers, G.W., Lansberg, M.G., Apr 2015. Apparent diffusion coefficient threshold for delineation of ischemic core. Int. J. Stroke 10 (3), 348–353.

Ray, K.J., Larkin, J.R., Tee, Y.K., Khrapitchev, A.A., Karunanithy, G., Barber, M., Baldwin, A.J., Chappell, M.A., Sibson, N.R., Nov 2016. Determination of an optimally sensitive and specific chemical exchange saturation transfer MRI quantification metric in relevant biological phantoms. NMR Biomed. 29 (11), 1624–1633.

Smith, S.M., Nov 2002. Fast robust automated brain extraction. Hum. Brain Mapp. 17 (3), 143–155.

Smith, S.M., Jenkinson, M., Woolrich, M.W., Beckmann, C.F., Behrens, T.E., Johansen-Berg, H., Bannister, P.R., De Luca, M., Drobnjak, I., Flitney, D.E., Niazy, R.K., Saunders, J., Vickers, J., Zhang, Y., De Stefano, N., Brady, J.M., Matthews, P.M., 2004. Advances in functional and structural MR image analysis and implementation as FSL. Neuroimage 23, S208–S219 Suppl 1.

Sun, P.Z., Zhou, J., Sun, W., Huang, J., van Zijl, P.C., Jun 2007. Detection of the ischemic penumbra using pH-weighted MRI. J. Cereb. Blood Flow Metab. 27 (6), 1129–1136.

Tee, Y.K., Khrapitchev, A.A., Sibson, N.R., Payne, S.J., Chappell, M.A., Sep 2012. Evaluating the use of a continuous approximation for model-based quantification of pulsed chemical exchange saturation transfer (CEST). J. Magn. Reson. 222, 88–95.

Tee, Y.K., Khrapitchev, A.A., Sibson, N.R., Payne, S.J., Chappell, M.A., Nov 2013. Optimal sampling schedule for chemical exchange saturation transfer. Magn. Reson. Med. 70 (5), 1251–1262.

Tee, Y.K., Harston, G.W., Blockley, N., Okell, T.W., Levman, J., Sheerin, F., Cellerini, M., Jezzard, P., Kennedy, J., Payne, S.J., Chappell, M.A., Sep 2014. Comparing different analysis methods for quantifying the MRI amide proton transfer (APT) effect in hyperacute stroke patients. NMR Biomed. 27 (9), 1019–1029.

Tee, Y.K., Harston, G.W., Blockley, N., Frost, R., Okell, T.W., Thandeswaran, S., Sheerin, F., Jezzard, P., Kennedy, J., Payen, J.F., Chappell, M., 2015. Can nuclear overhauser enhancement mediated chemical exchange saturation transfer (NOE CEST) offer a new insight in acute stroke diagnosis? Proc. Int. Soc. Mag. Reson. Med. 23, 17.

Vinogradov, E., Sherry, A.D., Lenkinski, R.E., Apr 2013. CEST: from basic principles to applications, challenges and opportunities. J. Magn. Reson. 229, 155–172.

Wang, Y., Zhang, Y., Zhao, X., Wu, B., Gao, J.H., 2017. Perturbation of longitudinal relaxation rate in rotating frame (PLRF) analysis for quantification of chemical exchange saturation transfer signal in a transient state. Magn. Reson. Med. 78 (5), 1711–1723.

Ward, K.M., Aletras, A.H., Balaban, R.S., Mar 2000. A new class of contrast agents for MRI based on proton chemical exchange dependent saturation transfer (CEST). J. Magn. Reson. 143 (1), 79–87.

Zaiss, M., Bachert, P., 2013a. Exchange-dependent relaxation in the rotating frame for slow and intermediate exchange – modeling off-resonant spin-lock and chemical exchange saturation transfer. NMR Biomed. 26 (5), 507–518 May.

Zaiss, M., Bachert, P., 2013b. Chemical exchange saturation transfer (CEST) and MR Z-spectroscopy in vivo: a review of theoretical approaches and methods. Phys. Med. Biol. 58 (22), R221–R269 Nov.

Zaiss, M., Kunz, J., Goerke, S., Radbruch, A., Bachert, P., Dec 2013. MR imaging of protein folding in vitro employing nuclear-Overhauser-mediated saturation transfer. NMR Biomed. 26 (12), 1815–1822.

Zaiss, M., Xu, J., Goerke, S., Khan, I.S., Singer, R.J., Gore, J.C., Gochberg, D.F., Bachert,

P., Mar 2014. Inverse Z-spectrum analysis for spillover-, MT-, and T1 -corrected steady-state pulsed CEST-MRI–application to pH-weighted MRI of acute stroke. NMR Biomed. 27 (3), 240–252.

Zaiss, M., Windschuh, J., Goerke, S., Paech, D., Meissner, J.E., Burth, S., Kickingereder, P., Wick, W., Bendszus, M., Schlemmer, H.P., Ladd, M.E., Bachert, P., Radbruch, A., Jan 2016. Downfield-NOE-suppressed amide-CEST-MRI at 7 tesla provides a unique contrast in human glioblastoma. Magn. Reson. Med. 77, 196–208.

Zhang, Y., Brady, M., Smith, S., Jan 2001. Segmentation of brain MR images through a hidden Markov random field model and the expectation-maximization algorithm. IEEE Trans. Med. Imaging 20 (1), 45–57.

Zhang, X.Y., Wang, F., Afzal, A., Xu, J., Gore, J.C., Gochberg, D.F., Zu, Z., Oct 2016. A new NOE-mediated MT signal at around -1.6ppm for detecting ischemic stroke in rat brain. Magn. Reson. Imaging 34 (8), 1100–1106.

Zhou, J., Payen, J.F., Wilson, D.A., Traystman, R.J., van Zijl, P.C., Aug 2003. Using the amide proton signals of intracellular proteins and peptides to detect pH effects in MRI. Nat. Med. 9 (8), 1085–1090.

Zhou, J., Hong, X., Zhao, X., Gao, J.H., Yuan, J., Aug 2013. APT-weighted and NOE-weighted image contrasts in glioma with different RF saturation powers based on magnetization transfer ratio asymmetry analyses. Magn. Reson. Med. 70 (2), 320–327.